CCIT Report # 404
November 2002

Image Enhancement and Denoising by Complex Diffusion Processes

Guy Gilboa, Yehoshua Y. Zeevi
Department of Electrical Engineering,
Technion - Israel Institute of Technology,
Technion City, Haifa 32000, ISRAEL

Nir Sochen
Department of Applied Mathematics,
University of Tel-Aviv
Ramat-Aviv, Tel-Aviv 69978, Israel

November 2002

Abstract

The linear and nonlinear scale spaces are generalized in the complex domain, by combining the diffusion equation with the simplified Schrödinger equation. A fundamental solution for the linear case is developed. Preliminary analysis of the complex diffusion shows that the generalized diffusion has properties of both forward and inverse diffusion. An important observation, supported theoretically and numerically, is that the imaginary part can serve as an edge detector (smoothed second derivative scaled by time), when the complex diffusion coefficient approaches the real axis. Based on this observation, we develop two nonlinear complex processes: a regularized shock filter for image enhancement and a ramp preserving denoising process.

1 Introduction

The scale-space approach is by now a well established multi-resolution technique for image structure analysis (see [24],[14],[21]). Originally, the Gaussian representation introduced a scale dimension by convolving the original image with a Gaussian of a standard deviation $\sigma = \sqrt{2t}$. This is analogous to solving the initial value problem of the linear diffusion equation

$$I_t = c\nabla^2 I, \quad I|_{t=0} = I_0, \quad 0 < c \in \mathbb{R}, \tag{1}$$

with a constant diffusion coefficient $c = 1$.

Perona and Malik (P-M) [19] proposed a nonlinear adaptive diffusion process, wherein diffusion takes place with a variable diffusion coefficient, in order to reduce the smoothing effect near edges. The P-M nonlinear diffusion equation is of the form: $I_t = \nabla \cdot (c(|\nabla I|)\nabla I), \quad c(\cdot) > 0$, where c is a decreasing function of the gradient. Our aim is to see if the linear and nonlinear scale-spaces can be viewed as special cases of a more general theory of complex diffusion-type processes.

Complex diffusion-type processes are encountered, for example in quantum physics and in electro-optics [6, 17]. The time dependent *Schrödinger equation* is the fundamental equation of quantum mechanics. In the simplest case of a particle without spin, subjected to an external field, it assumes the form

$$i\hbar\frac{\partial\psi}{\partial t} = -\frac{\hbar^2}{2m}\Delta\psi + V(x)\psi \quad , \tag{2}$$

where $\psi = \psi(t, x)$ is the wave function of a quantum particle, m is the mass of the particle, $\hbar$ is Planck's constant, $V(x)$ is the potential as a function of x, generating the external field, Δ denotes the Laplacian and $i \doteq \sqrt{-1}$. With an initial condition $\psi|_{t=0} = \psi_0(x)$, requiring that $\psi(t, \cdot) \in L_2$ for each fixed t, the solution is $\psi(t, \cdot) = e^{-\frac{i}{\hbar}tH}\psi_0$, where the exponent is a shorthand for the corresponding power series, and the higher order terms are defined recursively by $H^n\Psi = H(H^{n-1}\Psi)$. The operator

$$H = -\frac{\hbar^2}{2m}\Delta + V(x), \tag{3}$$

known as the *Schrödinger operator*, is interpreted as the energy operator of the particle under consideration. The first term is the kinetic energy and the second is the potential energy. The duality relations that exist between the Schrödinger equation and diffusion theory have been studied in [16]. Another important complex PDE in the field of phase transitions of traveling wave systems is the *complex Ginzburg-Landau equation* (CGL,[7]): $u_t = (1 + i\nu)u_{xx} + Ru - (1 + i\mu)|u|^2u$. Note that although these flows have a diffusion structure, because of the complex coefficient, they retain wave propagation properties.

In both cases a non-linearity is introduced by adding a potential term while the kinetic energy stays linear. In this study we employ the equation with zero potential (no external field) but with non-linear "kinetic energy". The role of the potential function in modeling and constraining the structure of textures, is investigated in a complementary study.

To better understand the complex flow, we study in Section 2 the linear case and derive the fundamental solution. We show that for small imaginary part of the complex diffusion coefficient, the flow is approximately a linear real diffusion for the real part, while the imaginary part behaves like a second derivative of the real part. Indeed, as expected, the imaginary part is directly related to the localized phase and, as such, to the zero crossings of the image. This is one of the important properties obtained by generalizing the diffusion approach to the complex case. The non-linear case is presented in Sections 3 and 4, where the intuition gained from the analysis of the linear case facilitates the development of two nonlinear complex schemes for denoising of ramps and for enhancement by regularized shock filters. The advantages over known real-valued PDE-based algorithms is demonstrated by means of one- and two-dimensional examples.

2 Linear Complex Diffusion

2.1 Problem Definition

We consider the following initial value problem:

$$\begin{aligned} I_t &= cI_{xx}, \qquad t > 0, \qquad x \in \mathbb{R} \\ I(x;0) &= I_0 \in \mathbb{R}, \quad c, I \in \mathbb{C}. \end{aligned} \tag{4}$$

This equation is a generalization of two equations: the linear *diffusion* equation (1) for $c \in \mathbb{R}$ and the simplified *Schrödinger* equation, i.e. $c \in \mathbb{I}$ and $V(x) \equiv 0$. When $c \in \mathbb{R}$ there are two cases: for $c > 0$ the process is a well posed forward diffusion, whereas for $c < 0$ an ill posed inverse diffusion process is obtained. In the general case the initial condition I_0 is complex. In this paper we discuss the particular case of real initial conditions, where I_0 is the original image.

2.2 The Fundamental Solution

We seek the complex fundamental solution $h(x;t)$ that satisfies the relation:

$$I(x;t) = I_0 * h(x;t), \tag{5}$$

where $*$ denotes convolution. We rewrite the complex diffusion coefficient as $c \doteq re^{i\theta}$. Since there does not exist a stable fundamental solution of the inverse diffusion process, let us restrict ourselves to a positive real value of c, that is $\theta \in (-\frac{\pi}{2}, \frac{\pi}{2})$. Replacing the real time variable t by a complex time $\tau = ct$, we get $I_\tau = I_{xx}$, $I(x;0) = I_0$. This is the linear diffusion equation with the Gaussian function being its fundamental solution. Reverting back to t, we get:

$$h(x;t) = \frac{C}{2\sqrt{\pi tc}} e^{-x^2/(4tc)}, \tag{6}$$

where $C \in \mathbb{C}$ is a constant calculated according to the initial conditions. Separating the real and imaginary exponents, we get:

$$\begin{aligned} h(x;t) &= \tfrac{Ce^{-i\theta/2}}{2\sqrt{\pi tr}} e^{-x^2\cos\theta/(4tr)} e^{ix^2\sin\theta/(4tr)} \\ &= CAg_\sigma(x;t)e^{i\alpha(x;t)}, \\ &\quad \text{where } g_\sigma(x;t) = \tfrac{1}{\sqrt{2\pi}\sigma(t)} e^{-x^2/2\sigma^2(t)}, \end{aligned}$$

and

$$A = \frac{1}{\sqrt{\cos\theta}}, \quad \alpha(x;t) = \frac{x^2\sin\theta}{4tr} - \frac{\theta}{2}, \quad \sigma(t) = \sqrt{\frac{2tr}{\cos\theta}}. \tag{7}$$

In order to satisfy the initial condition $I(x;0) = I_0$ we require

$$\begin{array}{lll} (a) & \int_{-\infty}^{\infty} h(x;t\to 0)dx = 1, & \text{that is} \\ & \int_{-\infty}^{\infty} \mathrm{Re}\{h(x;t\to 0)\}dx = 1, & \int_{-\infty}^{\infty} \mathrm{Im}\{h(x;t\to 0)\}dx = 0, \\ (b) & \int_{|x|>\epsilon} |h(x;t\to 0)|dx \to 0, & \text{where } \epsilon = \epsilon(t),\ \lim_{t\to 0}\epsilon(t) = 0. \end{array} \tag{8}$$

This leads to $C = 1$ (a detailed proof is in the appendix). The fundamental solution is therefore:

$$h(x;t) = Ag_\sigma(x;t)e^{i\alpha(x;t)}, \tag{9}$$

with the scalar A, the Gaussian's standard deviation σ and the exponent function α as in (7).

Note that the constant C (and consequently Eq. (9)) derived above is different than the one in [13]. This correction is a consequence of the explicit initial conditions requirements formulated in (8).

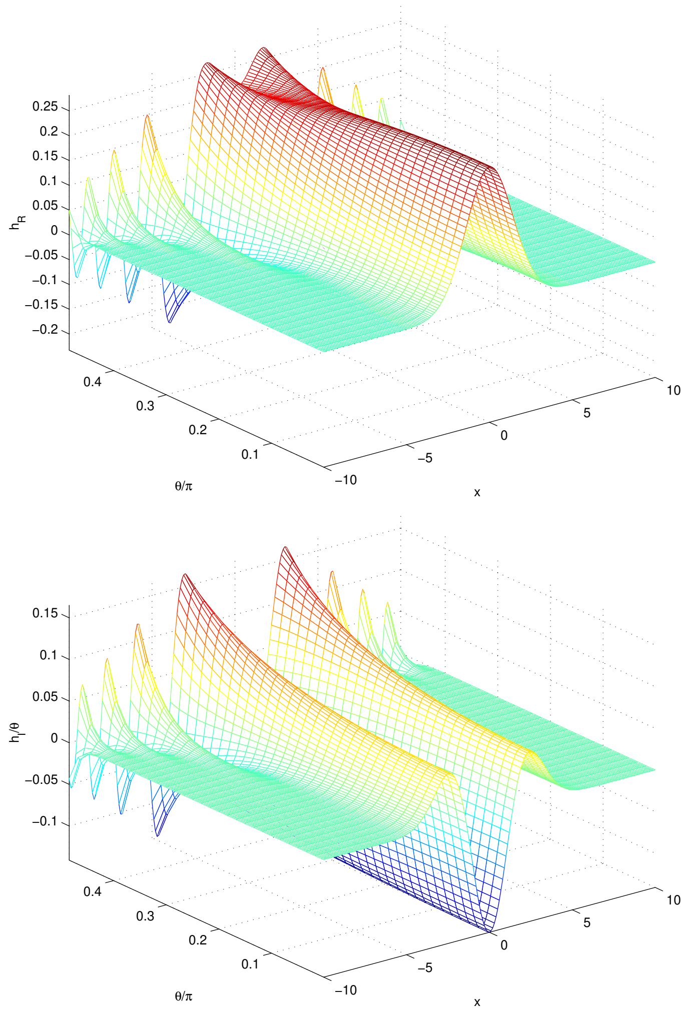

Figure 1: Fundamental solution $h_\theta(x;t)$ as a function of x and θ ($t = 1$). Left - real part (h_R), right - imaginary part normalized by θ (h_I/θ).

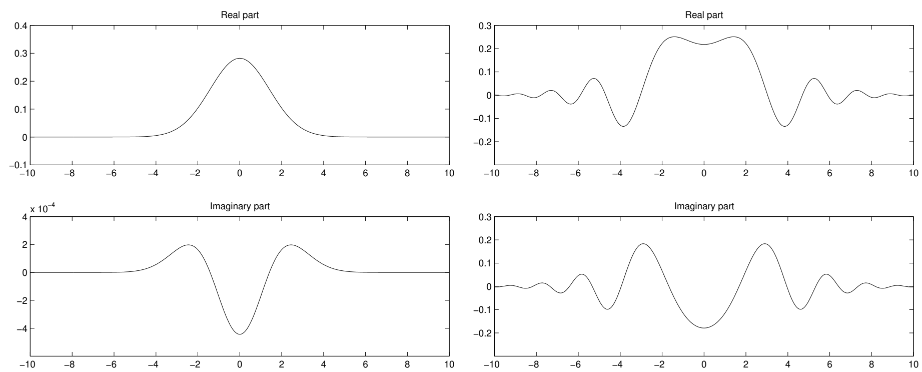

Figure 2: Fundamental solution $h(x;t)$ as a function of x for small and large values of theta ($t=1$). Left - small theta ($\theta=\pi/1000$), right - large theta ($\theta=7\pi/16$). Top frames - real part, bottom frames - imaginary part.

2.3 Approximate Solution for Small Theta

We will now show that as $\theta \to 0$, the imaginary part can be regarded as a smoothed second derivative of the initial signal, factored by θ and the time t. Generalizing the solution to any dimension with Cartesian coordinates $\mathbf{x} \doteq (x_1, x_2, ..x_N) \in \mathbb{R}^N$, $I(\mathbf{x};t) \in \mathbb{C}^N$, and denoting that in this coordinate system $\mathbf{g}_\sigma(\mathbf{x};t) \doteq \prod_i^N g_\sigma(x_i;t)$, we show that:

$$\lim_{\theta\to 0} \frac{Im(I)}{\theta} = t\Delta \mathbf{g}_{\tilde{\sigma}} * I_0, \tag{10}$$

where $Im(\cdot)$ denotes the imaginary value and $\tilde{\sigma} = lim_{\theta\to 0}\sigma = \sqrt{2t}$. For convenience we use here a unit complex diffusion coefficient $c = e^{i\theta}$, and utilize the following approximations for small θ: $cos\theta = 1 + O(\theta^2)$ and $sin\theta = \theta + O(\theta^3)$. Introducing an operator $\tilde{H}$, which is similar to the *Schrödinger operator*, we can write equation (4) (in any dimension) as: $I_t = \tilde{H}I$; $I|_{t=0} = I_0$, where $\tilde{H} = c\Delta$. The solution $I = e^{t\tilde{H}}I_0$, is the equivalent of (5) and (9). Using the above approximations we get:

$$\begin{aligned} I(\mathbf{x},t) &= e^{ct\Delta}I_0 = e^{e^{i\theta}t\Delta}I_0 \\ &\approx e^{(1+i\theta)t\Delta}I_0 = e^{t\Delta}e^{i\theta t\Delta}I_0 \\ &\approx e^{t\Delta}(1+i\theta t\Delta)I_0 = (1+i\theta t\Delta)\mathbf{g}_{\tilde{\sigma}} * I_0. \end{aligned}$$

A thorough analysis of the approximation error is currently being studied. Numerical experiments show that values of $\theta < 1^\circ = \pi/180$ produce satisfactory results. It is important to point out that empirically the Gaussian scale-space zero crossing location is preserved. Resorting to the presentation technique of Witkin [24], we present in Fig. 5 evolution of the zero-crossings of the second derivative of a real diffusion process versus the imaginary value zero-crossing of the complex diffusion. It is observed that the behavior is very similar (for small θ).

Some further insight into the behavior of the small-theta approximation can be gained by separating the real and imaginary parts of the signal, $I = I_R + iI_I$, and diffusion coefficient, $c = c_R + ic_I$, into a set of two equations:

$$\begin{cases} I_{Rt} & = c_R I_{Rxx} - c_I I_{Ixx} \quad , I_R|_{t=0} = I_0 \\ I_{It} & = c_I I_{Rxx} + c_R I_{Ixx} \quad , I_I|_{t=0} = 0, \end{cases} \tag{11}$$

where $c_R = \cos\theta$, $c_I = sin\theta$. The relation $I_{Rxx} \gg \theta I_{Ixx}$ holds for small enough θ, which allows us to omit the second term on the r.h.s. of the first equation, to get the small theta approximation:

$$I_{Rt} \approx I_{Rxx} \quad ; \qquad I_{It} \approx I_{Ixx} + \theta I_{Rxx}. \tag{12}$$

In (12) I_R is controlled by a linear forward diffusion equation, whereas I_I is affected by both the real and imaginary equations. We can regard the imaginary part as $I_{It} \approx \theta I_{Rxx} +$ ("a smoothing process"). Here θI_{Rxx} is the dominant part as $I_I|_{t=0} = 0$.

2.4 Examples

We present examples of 1D and 2D signal processing with complex diffusion processes characterized by small and large values of θ. In Fig.'s (3) and (4), a unit step is processed with small and large θ ($\frac{\pi}{30}, \frac{14\pi}{30}$ respectively). The same θ values are used in the processing of the the cameraman image (Fig.'s. (6) and (7), respectively). The qualitative properties of the edge detection (smoothed second derivative) are clearly apparent in the imaginary part of the signals, for the small θ value, whereas the real value depicts the properties of ordinary Gaussian scale-space. For large θ, however, the imaginary part feeds back into the real part significantly, creating wave-like ringing. In addition, the signal overshoots and undershoots, exceeding the original maximum and minimum values and thereby violating the "Maximum-minimum" principle – a property suitable for sharpening purposes, similar to the Mach Bands characteristic of vision [22].

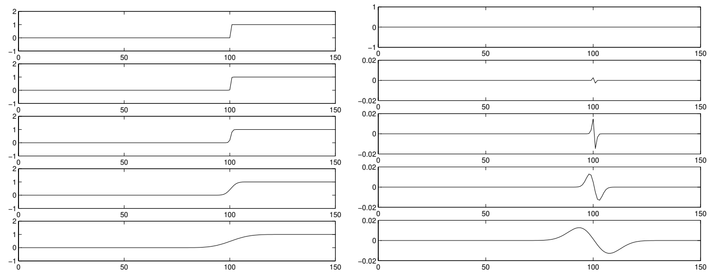

Figure 3: Complex diffusion of a small theta, $\theta = \pi/30$, applied to a step signal. Left frame - real values, right frame - imaginary values. Each frame depicts from top to bottom: original step, diffused signal after times: 0.025, 0.25, 2.5, 25.

2.5 Generalization to Nonlinear Complex Diffusion

Nonlinear complex processes can be derived from the above-mentioned properties of the linear complex diffusion. In the following sections we present two nonlinear schemes, developed for application in image denoising and enhancement.

3 Ramp Preserving Denoising

Consider the following example of a nonlinear process, developed for the purpose of denoising ramp-type edges. Note that the ramp-type edge calls for different processing from the widely-used methods applied in the case of step-type (singular) edges. We are looking for a general nonlinear diffusion equation

$$I_t = \frac{\partial}{\partial x}\left(c(\cdot) I_x\right) \tag{13}$$

that preserves smoothed ramps. Following the same logic that utilized a gradient measure in order to slow the diffusion near step edges, we search for a suitable differential operator $\mathcal{D}$ for ramp edges. Eq. (13) with a diffusion coefficient $c(|\mathcal{D}I|)$ which is a decreasing function of $|\mathcal{D}I|$ can be regarded as a ramp preserving process. Examining the gradient, as a possible candidate, leads to the conclusion that it is not a suitable measure for two reasons: The gradient does not detect the ramp main features - namely its endpoints;

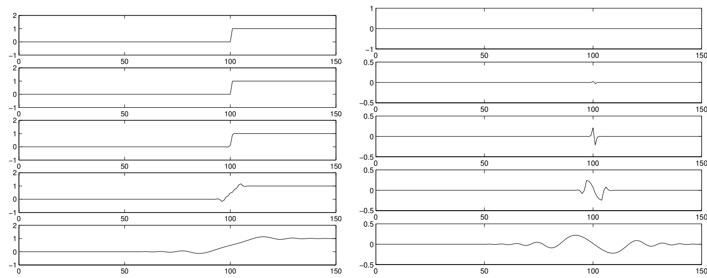

Figure 4: Complex diffusion of a large theta, $\theta = 14\pi/30$, applied to a step signal. Left frame - real values, right frame - imaginary values. Each frame depicts from top to bottom: original step, diffused signal after times: 0.025, 0.25, 2.5, 25.

Moreover, it has a nearly uniform value across the whole smoothed ramp, causing a nonlinear gradient-dependent diffusion to slow the diffusion process in that region, thus not being able to properly reduce noise within a ramp (creating staircasing effects). The second derivative (Laplacian in more than one dimension) is a suitable choice: It has a high magnitude near the endpoints and low magnitude elsewhere, and thus enables the nonlinear diffusion process to reduce noise during the occurrence of a ramp.

We formulate $c(s)$ as a decreasing function of s:

$$c(s) = \frac{1}{1+s^2}, \text{ where } c(s) = c(|I_{xx}|), \tag{14}$$

and apply it in (13) to yield:

$$I_t = \frac{\partial}{\partial x}\left(\frac{I_x}{1+I_{xx}^2}\right) = \frac{1+I_{xx}^2 - 2I_x I_{xxx}}{(1+I_{xx}^2)^2} I_{xx}. \tag{15}$$

There are two main problems in this scheme. The first and more important one is the fact that noise has very large (theoretically unbounded) second derivatives. Secondly, a numerical problem arises as third derivatives should be computed, with large numerical support and noisier derivative estimations. These two problems are solved by using the nonlinear complex diffusion.

Following the results of the linear complex diffusion (Eq. 10), we estimate by the imaginary value of the signal (divided by θ) the smoothed second derivative multiplied by the time t.

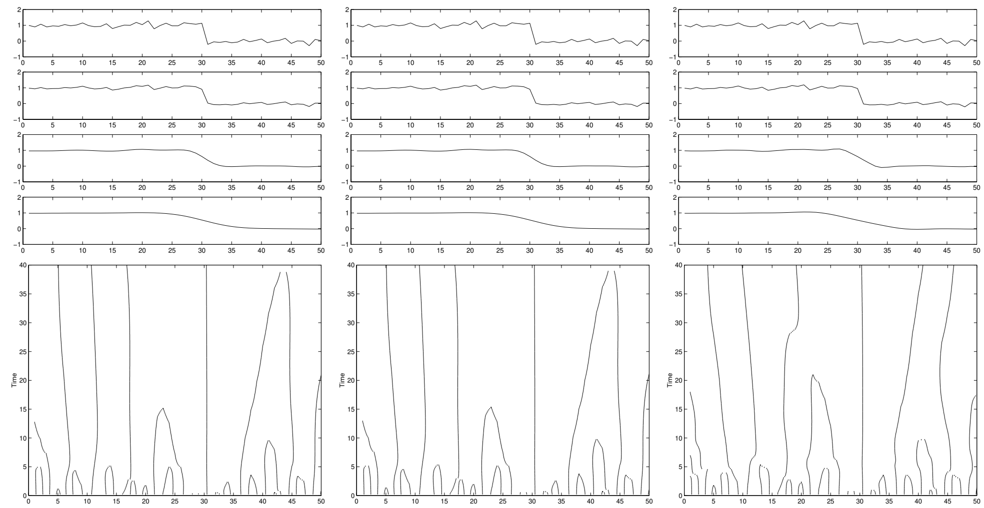

Figure 5: Comparison of linear real and complex diffusion processes applied to a noisy step signal. Top frames depict (from top to bottom): original signal, diffused signal after times: 0.25, 2, 10. Bottom frames portray the evolution of the zero-crossing locations as a function of time. Top frames (from left): real diffusion, real value of complex diffusion $\theta = \pi/1000$, real value of complex diffusion $\theta = \pi/10$; Bottom frames: zero-crossing of the second derivative of the signal corresponding to real value, imaginary value of $\theta = \pi/1000$, and imaginary value of $\theta = \pi/10$, respectively.

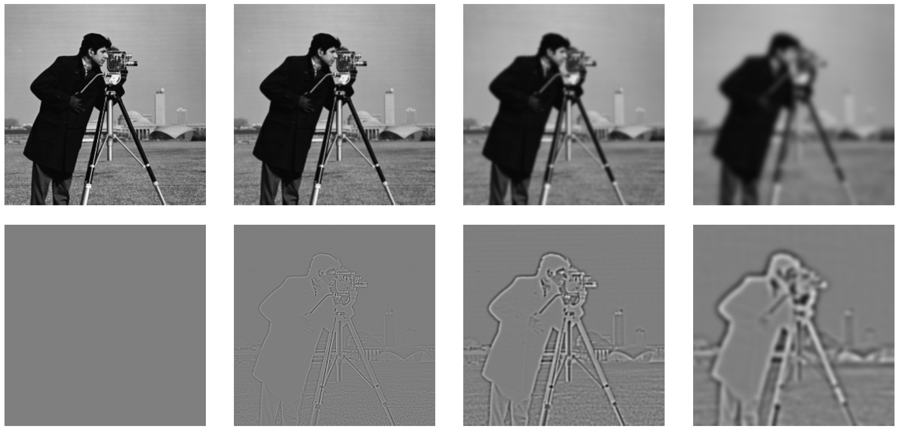

Figure 6: Complex diffusion with small theta ($\theta = \pi/30$), applied to the cameraman image. Top images – real values, bottom images – imaginary values (factored by 20). Each frame (from left to right): original image, result obtained after processing time 0.25, 2.5, 25, respectively.

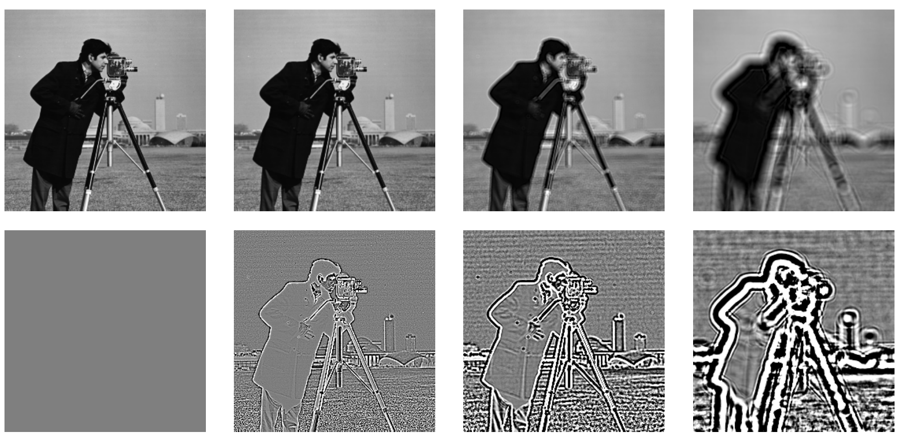

Figure 7: Complex diffusion with large theta ($\theta = 14\pi/30$), applied to the cameraman image. Top sequence of images – real values, bottom sequence – imaginary values (factored by 20). Each sequence depicts from left to right the original image and the results of the processing after t=0.25, 2.5, and 25, respectively.

Whereas for small t this terms vanish, allowing stronger diffusion to reduce the noise, with time its influence increases and preserves the ramp features of the signal. We should comment that this type of second derivative estimation (i.e. nonlinear-based) is more biased than the one based on linear processing; The bias in this case is a direct consequence of the application of a nonlinear process.

The equation for the multidimensional process is

$$\begin{aligned} I_t &= \nabla \cdot (c(Im(I))\nabla I), \\ c(Im(I)) &= \frac{e^{i\theta}}{1 + \left(\frac{Im(I)}{k\theta}\right)^2} \end{aligned} \tag{16}$$

where k is a threshold parameter. For the same reasons as those discussed in the linear case, here too the phase angle θ should be small ($\theta << 1$). Since the imaginary part is normalized by θ, the process is not affected much by changing the value of θ as long as it stays small.

We implement this flow with forward Euler scheme, using central difference approximation for the spatial derivatives and backward time derivative. Care should be exercised in this implementation in determining what the time step should be. As discussed earlier, the fundamental solution includes a Gaussian-type kernel of variance $\sigma^2 = \frac{2tr}{\cos\theta}$. Implementing Gaussian convolution of time τ, by incremental time steps where $\sigma^2 = 2\tau$, requires the time step bound to be: $\Delta\tau \le 0.25h^2$ (in 2 dimensions, where h is the spatial step). Here we have $\tau = \frac{tr}{\cos\theta}$ and hence in the general case we require: $\Delta t \le 0.25h^2 \frac{\cos\theta}{r}$, and for our case where $r = 1$, $h = 1$: $\Delta t \le 0.25\cos\theta$. Thus, when θ approaches $\pi/2$ it becomes very inefficient to implement complex diffusion with incremental time-steps. For small θ, however, there is essentially no difference from the case of real diffusion.

In Figs. 8 and 9 we compare denoising of a ramp signal by a P-M process, with the performance of the above process (Eq. 16). This example illustrates that the staircasing effect, characteristic of the P-M process, does not occur in processing by our nonlinear complex scheme. This important difference is further substantiated by the results of processing of images that contain both sharp (i.e. step-type) and soft (i.e. ramp-type) edges, such as the one illustrated in Fig. 10. Note that using the regularized version of the P-M process, proposed by Catte et al. [4], produces staircasing results similar to those generated by the original P-M process.

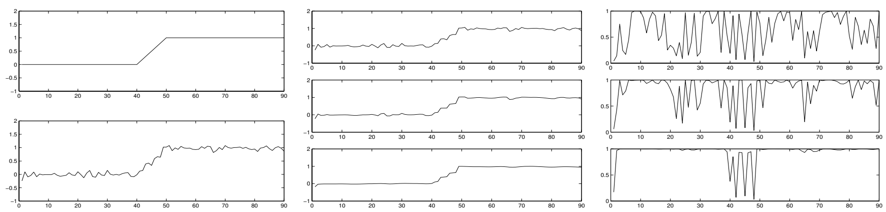

Figure 8: Perona-Malik nonlinear diffusion process applied to a ramp-type soft edge ($k = 0.1$). Left - original (top) and noisy ramp signal (white Gaussian, SNR=15dB) . Middle - denoised signal at times $0.25, 1, 2.5$, from top to bottom, respectively. Right - respective values of c coefficient.

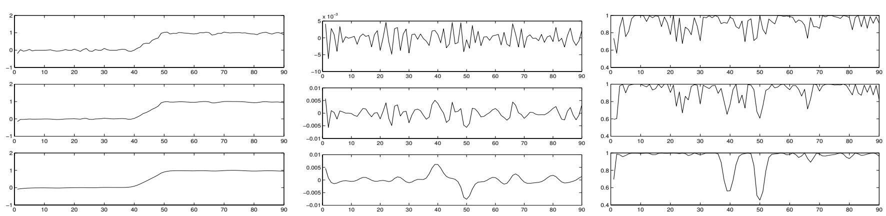

Figure 9: Nonlinear complex diffusion process applied to a ramp-type soft edge ($\theta = \pi/30$, $k = 0.07$). Left - real values of denoised signal at times $0.25, 1, 2.5$, from top to bottom, respectively. Middle - respective imaginary values, right - respective real values of c.

4 Regularized Shock Filters

Most of the research concerning the application of partial differential equations in the fields of computer vision and image processing focused on parabolic (diffusion-type) equations. In [18] Osher and Rudin proposed a hyperbolic equation called shock filter that can serve as a stable deblurring algorithm approximating deconvolution.

4.1 Problem Statement

The formulation of the shock filter equation is:

$$I_t = -|I_x| F(I_{xx}), \tag{17}$$

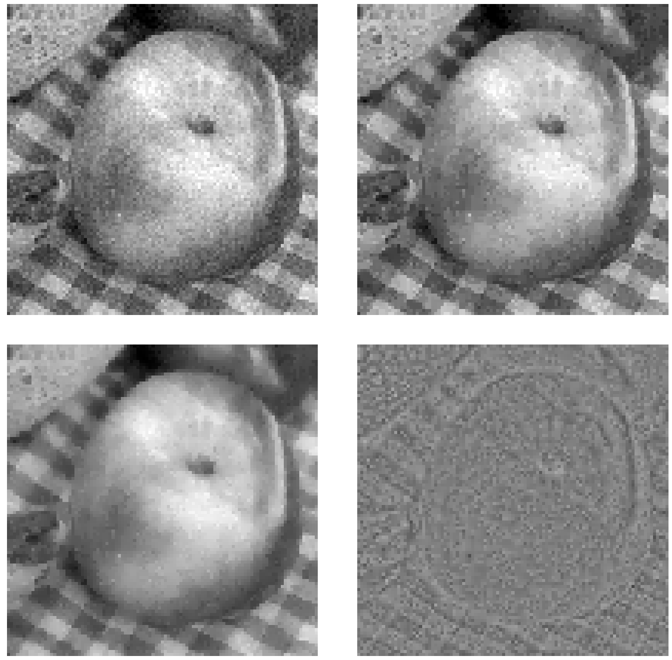

Figure 10: Nonlinear diffusion of an apple image: Top: left - image corrupted by white Gaussian noise (SNR=13dB), right - image denoised by Perona-Malik process ($k = 3$,$time = 2.5$). Bottom: image denoised by complex nonlinear scheme ($\theta = \pi/30$, $k = 2$, $time = 2.5$), left - real part, right - imaginary part. One can see that the apple is better denoised in the complex scheme, where staircasing effects appear in the P-M process. Trying to increase the P-M threshold in order to avoid staircasing causes the whole apple to get diffused with the background. Another observation is that the complex scheme denoises faster (due to its implicit time dependency).

where F should satisfy $F(0) = 0$, and $F(s)\text{sign}(s) \geq 0$. Note: the above equation and all other evolutionary equations in this section have initial conditions $I(x, 0) = I_0(x)$ and Neumann boundary conditions ($\frac{\partial I}{\partial n} = 0$ where n is the direction perpendicular to the boundary).

Choosing $F(s) = \text{sign}(s)$ yields the classical shock filter equation:

$$I_t = -\text{sign}(I_{xx})|I_x|, \tag{18}$$

generalized in the 2D case to:

$$I_t = -\mathrm{sign}(I_{\eta\eta})|\nabla I|, \tag{19}$$

where η is the direction of the gradient.

The 1D process (Eq. 18) is approximated by the following discrete scheme:

$$I_i^{n+1} = I_i^n - \Delta t|DI_i^n|\mathrm{sign}(D^2 I_i^n), \tag{20}$$

where

$$\begin{aligned} DI_i^n &\doteq m(\Delta_+ I_i^n, \Delta_- I_i^n)/h, \\ D^2 I_i^n &\doteq (\Delta_+ \Delta_- I_i^n)/h^2, \end{aligned} \tag{21}$$

$m(x, y)$ is the minmod function:

$$m(x,y) \doteq \begin{cases} \mathrm{sign}(x)\min(|x|,|y|); & \text{if } xy > 0, \\ 0 & \text{otherwise}, \end{cases}$$

and $\Delta_\pm \doteq \pm(u_{i\pm 1} - u_i)$. The CFL condition in the 1D case is $\Delta t \leq 0.5h$.

The shock filter main properties are:

- Shocks develop at inflection points (zero crossings of second derivative).
- Local extrema remain unchanged in time. No new local extrema are created. The scheme is total-variation-preserving (TVP).
- The steady state (weak) solution is piecewise constant (with discontinuities at the inflection points of I_0).
- The process approximates deconvolution.

Most rigorous analysis and proofs of these properties were based on the discrete scheme (Eq. 20).

As noted already in the original paper, any noise in the blurred signal will also be enhanced. As a matter of fact this process is extremely sensitive to noise. Theoretically, in the continuous domain, any white noise added to the signal may add an infinite number of inflection points, disrupting the process completely. Discretization may help somewhat, but in general the same sensitivity to noise occurs. This is illustrated by comparison of the processing of a noiseless and a noisy sine wave signals (Fig. (11)). Whereas in the case of a noiseless signal the shock filter well enhances the edges, turning a sine wave into a square-wave signal, in the noisy case - the shock filter does not enhance the edges at all, and the primary result of the processing is noise amplification, although only a very low level of white Gaussian noise was added to the input signal (SNR=40dB).

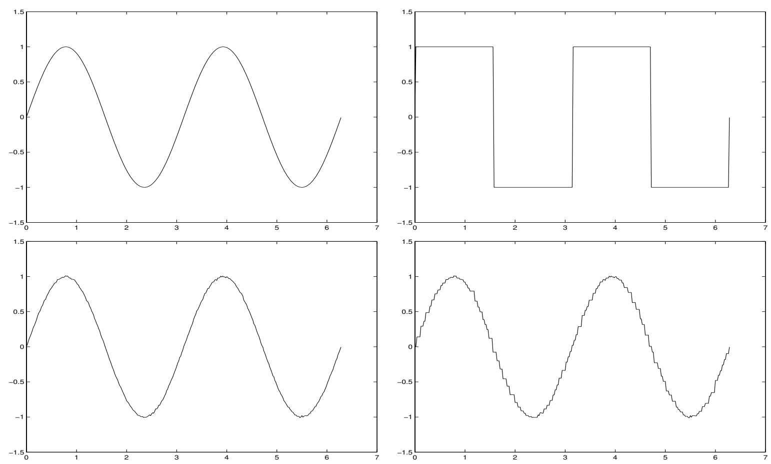

Figure 11: Noiseless sine wave signal (top left) and the steady state of its processing by a shock filter (top right), compared with the processing of a noisy signal, generated by adding low level of white Gaussian noise– SNR=40dB (bottom left). The steady state of the processed noisy signal does not depict any enhancement and the only result is noise amplification (bottom right).

4.2 Previous Related Studies

The noise sensitivity problem is critical and, unless properly solved, will continue to hinder most practical applications of shock filters. Previous studies addressing this issue came up with several possible solutions. The common approach to increase robustness ([1, 5, 15, 23]), is to convolve the signal's second derivative with a lowpass filter, such as a Gaussian:

$$I_t = -\mathrm{sign}(G_\sigma * I_{xx})|I_x|, \tag{22}$$

where G_σ is a Gaussian of standard deviation σ.

This is generally not sufficient to overcome the noise problem: convolving the signal with a Gaussian of moderate width, does not cancel in many cases the inflection points produced by the noise; Their magnitude becomes considerably lower, but there is still a change of sign at these points, which induces flow in opposite direction on each side of the inflection point. For very wide (large scale) Gaussians, most inflection points produced by the noise are diminished, but at a cost: the location of the signal's inflection points become less accurate. Moreover, the effective Gaussian's width σ is in many cases larger than the length of the signal, thus causing the boundary conditions imposed on the process to strongly affect the solution. Lastly, from a computational point of view, the convolution process in each iteration is costly.

A more complex approach, is to address the issue as an enhancing-denoising problem: smoother parts are denoised, whereas edges are enhanced and sharpened. The main idea is to add some sort of anisotropic diffusion term with an adaptive weight between the shock and the diffusion processes. Alvarez and Mazorra were the first to couple shock and diffusion, proposing an equation of the form [1]:

$$I_t = -\mathrm{sign}(G_\sigma * I_{\eta\eta})|\nabla I| + cI_{\xi\xi}, \tag{23}$$

where c is a positive constant and ξ is the direction perpendicular to the gradient ∇I. This equation, though, degenerates to (22) in the 1D case and the diffusion part is lost.

A somewhat similar scheme, was proposed by Kornprobst et al. [15]:

$$I_t = \alpha_r(h_\tau I_{\eta\eta} + I_{\xi\xi}) - \alpha_e(1 - h_\tau)\mathrm{sign}(G_\sigma * I_{\eta\eta})|\nabla I|, \tag{24}$$

where $h_\tau = h_\tau(|G_{\tilde\sigma} * \nabla I|) = 1$ if $|G_{\tilde\sigma} * \nabla I| < \tau$, and 0 otherwise. The original scheme includes another fidelity term $\alpha_f(I - I_0)$ that is omitted here (as such a term can be added to any scheme).

The process proposed by Coulon and Arridge [5],

$$I_t = \mathrm{div}(c\nabla I) - (1 - c)^\alpha \mathrm{sign}(G_\sigma * I_{\eta\eta})|\nabla I|, \tag{25}$$

where $c = \exp(-\frac{|G_{\tilde\sigma} * \nabla I|^2}{k})$, was originally used for classification, based on a probabilistic framework. Eq. (25) is the adaptation of the original process for direct processing of images.

The performance of these schemes will be later compared with that of the process proposed by us.

4.3 The magnitude of the second derivative

To account for the magnitude of the second derivative controlling the flow, we return to the original shock filter formulation of (17) and employ $F(s) = \frac{2}{\pi}\arctan(as)$, where a is a parameter that controls the sharpness of the slope near zero. This 'soft-sign' function is similar to the logistic function, widely used in neural networks. With this $F(s)$, Eq. (11) becomes:

$$I_t = -\frac{2}{\pi}\arctan(aI_{xx})|I_x| + \lambda I_{xx}. \tag{26}$$

Consequently, the inflection points are not of equal weight any longer; regions near edges, with large magnitude of the second derivative near the zero crossing, are sharpened much faster than relatively smooth regions.

4.4 Incorporating time dependency into the process

Another desirable goal is to have an adaptive process behavior, wherein the processing characteristics vary as a function of time in a controlled manner. This can be accomplished by explicitly incorporating time into Perona-Malik-type schemes [10], [19]. The basic idea is that processes controlled by the gradient magnitude have large errors in estimating gradients at the initial stages, where the signal is still very noisy. Therefore it is advantageous to emphasize the noise filtering during the initial phase of the processing. In [10] we presented two processes with continuous transition in time, beginning with linear diffusion at time zero (primarily denoising), advancing towards high nonlinearity (emphasizing edge-preserving properties).

Similar ideas can be applied here too. We would like to decrease the shock effects of the process at the beginning (when estimating the signal's inflection points is difficult), allowing the diffusion process to smooth out the noise. As the signal further evolves, false inflection points produced by the noise are greatly reduced and the enhancing 'shock treatment' predominates. A simple way to induce this type of transition in processing properties is to multiply the second derivative of the shock component by the time t:

$$I_t = -\frac{2}{\pi}\arctan(aI_{xx}t)|I_x| + \lambda I_{xx}. \tag{27}$$

This type of process will be implemented in a new complex PDE formulation.

4.5 Complex Shock Filters

From (27) and (10) we derive the complex shock filter formulation for small θ:

$$I_t = -\frac{2}{\pi}\arctan(a\mathrm{Im}(\frac{I}{\theta}))|I_x| + \lambda I_{xx}, \tag{28}$$

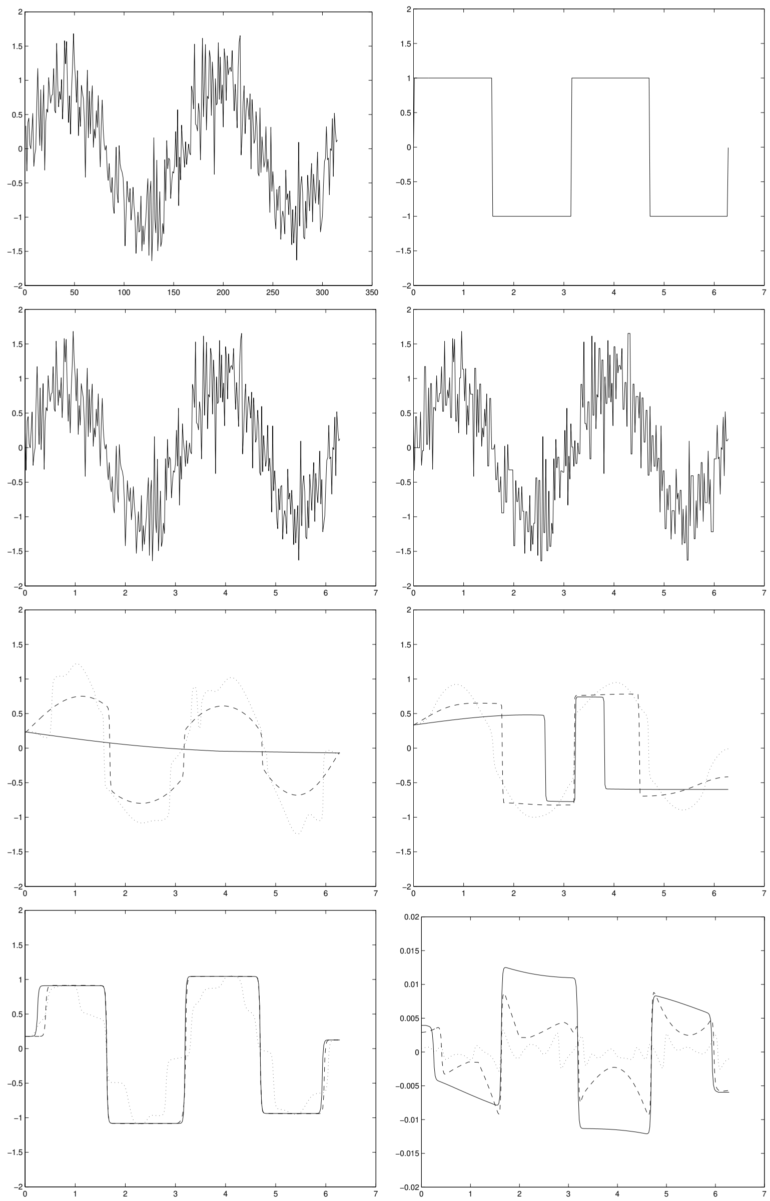

Figure 12: Noisy sine wave signal processed by several algorithms. From top, left: signal with additive white Gaussian noise (SNR=5dB), right: ideal steady state shock result; left: steady state of original shock filter Eq. (18), right: steady state of Eq. (22) - Gaussian convolved derivative, $\sigma = 100$; left: evolution of Eq. (24) - Kornprobst et al. ($\alpha_r = 1, \alpha_e = 0.5, \tau = 0.04, \sigma = 30, \tilde{\sigma} = 5$), right: evolution of Eq. (25) - Coulon-Arridge ($k = 0.01, \alpha = 1, \sigma = 30, \tilde{\sigma} = 5$); bottom: evolution of Eq. (28) - complex shock filter (our proposed scheme), left: real values, right: imaginary values, ($|\lambda| = 0.5, a = 5$). All evolution graphs depict 3 time points along the evolution: 300 (dotted), 3,000 (dashed) and 30,000 (solid) iteration.

where $\lambda = re^{i\theta}$is a complex scalar. Equation (28) is implemented by the same discrete approximations (except that all computations are complex); the CFL condition in 1D is $\Delta t \leq 0.5h^2 \frac{\cos\theta}{r}$.

Generalization of the complex shock filter to 2D yields:

$$I_t = -\frac{2}{\pi}\arctan(a\mathrm{Im}(\frac{I}{\theta}))|\nabla I| + \lambda I_{\eta\eta} + \tilde{\lambda} I_{\xi\xi}, \quad (29)$$

where $\tilde{\lambda}$ is a real scalar.

The complex filter is an elegant way to avoid the need for convolving the signal in each iteration and still get smoothed estimations. The time dependency of the process is inherent, without the need to explicitly use the evolution time t. Moreover, the imaginary value receives feedback– it is smoothed by the diffusion and enhanced at sharp transitions by the shock and, thus, can better control the process than a simple second derivative.

To illustrate the advantages afforded by the processing with the complex shock filter, its performance in processing of noisy sine wave signals is compared with those of the shock filters described earlier (Fig. 12). The original shock filter (Eq. (18)) and the one with Gaussian-convolved second derivative (Eq. (22)) are clearly not suitable for this task. The process of Kornprobst et al. (Eq. (24)) performs relatively well but the minimum and maximum of the signal decay quite fast and the deblurring is not so profound. Moreover there are 5 parameters that need to be adjusted and from our experience the performance of the process is quite sensitive to a few of them (especially to τ). The process of Coulon and Arridge (Eq. (25)) behaves somewhat better in this 1D example; it produces shock structures but is strongly affected by the boundary conditions and tends to move the shocks towards the center. Our complex shock filter scheme (Eq. (28)) seems to produce the best result, compared to the ideal result shown at the top right. The scheme is stable in time, decays slowly and well preserves the location of the shocks. Another advantage of our scheme is that we basically have only two parameters: $|\lambda|$ and a (in the 1D case, three in 2D). Note that as the process is normalized, it is not affected by the exact value of θ as long as it is small. In all our experiments we took $\theta = 0.01$. At the bottom right we can see the imaginary value of the complex process (the scale is 100 times smaller). One can see that the zero crossings are at the inflection points and that the energy of the imaginary value energy grows with time, thus enabling good preservation of the shocks.

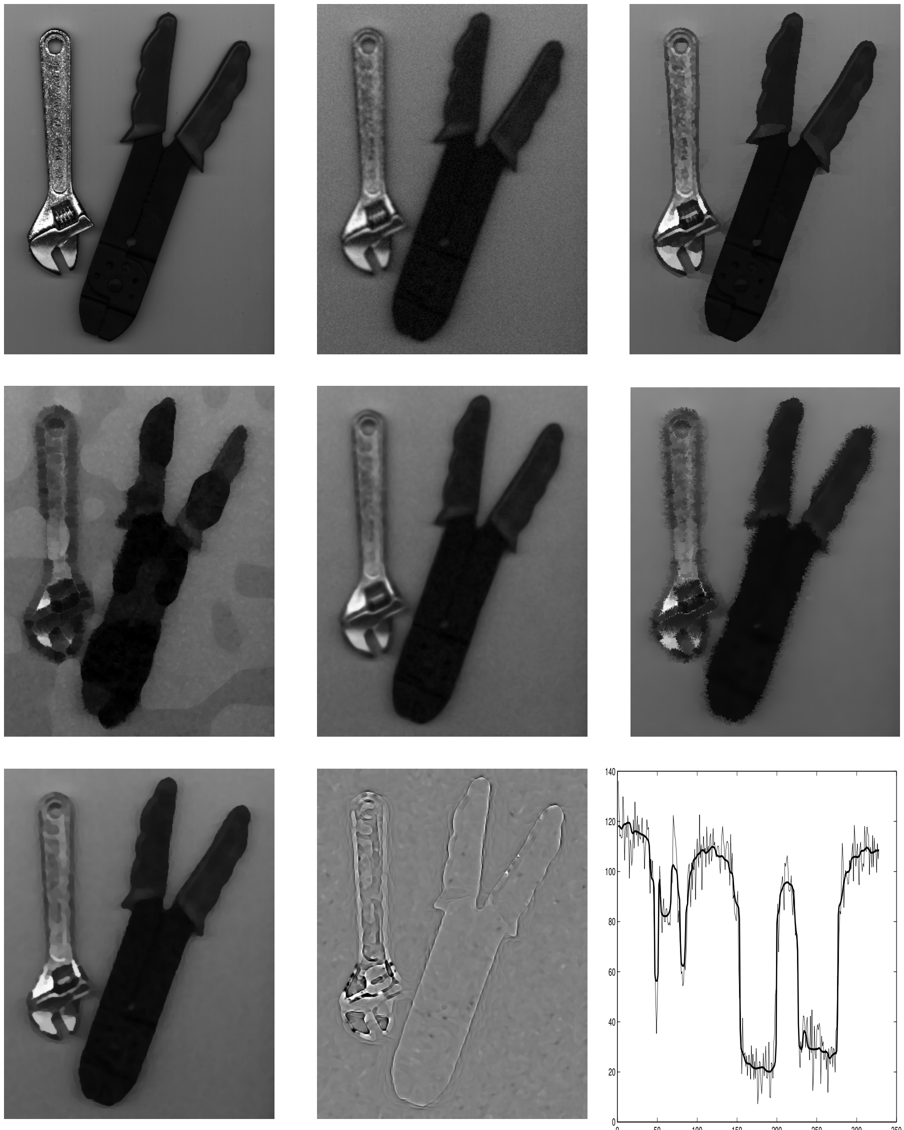

Figure 13: Top row (from left): Original tools image, Gaussian blurred ($\sigma = 2$) with added white Gaussian noise (SNR=15dB), ideal shock response (of blurred image without the noise); middle row: evolutions of Eq. (23) - Alvarez-Mazorra ($\sigma = 10$), Eq. (24) - Kornprobst et al. ($\alpha_r = 0.2, \alpha_e = 0.1, \tau = 0.2, \sigma = 10, \tilde{\sigma} = 1$), Eq. (25) - Coulon-Arridge ($k = 5, \alpha = 1, \sigma = 10, \tilde{\sigma} = 1$); bottom: evolution of Eq. (28) - complex process, left: real values, middle: imaginary values ($|\lambda| = 0.1, \tilde{\lambda} = 0.5, a = 0.5$), right: grey level values generated along a horizontal line in the course of complex evolution of the process (thin line 1 iteration; bold line 100 iterations). All of the image evolution results are presented for 100 iterations (dt=0.1).

In Fig. 13 a blurred and noisy tools image is processed. In the case of two dimensional signals, only the scheme of Kornprobst et at. and our complex scheme produce acceptable results at this levels of noise (Fig. 13). Processing with the complex process results, however, in sharper edges and is closer to the shock process, as can be observed in a comparison to an ideal shock response to a blurred image without noise (top-right image of Fig. 13). The combined enhancement-denoising properties of the complex scheme are highlighted by the display of one horizontal line of the image (bottom right of Fig. 13).

5 Concluding remarks and discussion

Generalization of the linear and nonlinear scale spaces to the complex domain, by combining the diffusion equation with the simplified Schrödinger equation, further enhances the theoretical framework of the diffusion-type PDE approach to image processing. The fundamental solution of the linear complex diffusion indicates that there exists a stable process over the wide range of the angular orientation of the complex diffusion coefficient, $\theta \in (-\frac{\pi}{2}, \frac{\pi}{2})$, that restricts the real value of the coefficient to be positive. [Issues related to aspects of inverse diffusion in image processing, i.e. negative real-valued diffusion coefficient, are dealt with elsewhere [11].]

In the case of small θ, two observations concerning the properties of the real and imaginary components of the complex diffusion process are relevant with regard to the application of this process in image processing: The real function is effectively decoupled from the imaginary one, and behaves like a real linear diffusion process, whereas the imaginary part approximates a smoothed second derivative of the real part, and can therefore well serve as an edge detector. In other words, the single complex diffusion process generates simultaneously an approximation of both the Gaussian and Laplacian pyramids [3] (at discrete set of temporal sampling points), i.e. the scale-space.

Although the nonlinear scheme remains to be further analyzed and better understood, nonlinear complex diffusion-type processes can be derived from the properties of the complex linear diffusion, and applied in image processing and enhancement. Such are the two nonlinear complex schemes developed for denoising of ramp edges and for regularization of shock filters. In the first scheme, the nonlinear complex diffusion process avoids the staircasing effect that is characteristic of the P-M process [19] and of the regularized version of the P-M process proposed by Catte et al. [4]. (See Figures 8, 9 and 10). The second proposed scheme, presents a complex shock filter that overcomes problems inherent in the enhancement of noisy signals and images by the shock filters [18] and its various variants [1, 5, 15, 23]. The complex scheme sharpens signals and images similarly to the ideal shock response, even under noisy conditions that either minimize or eliminate the shock effect in the case of application of one of the variants of the shock scheme. Under such noisy conditions, the original Osher-Rudin shock filter does not enhance the signal at all and even even further degrades it (insofar as the SNR condition is concerned, see Fig. 11).

Generalization of the linear and nonlinear scale spaces by combining the diffusion equation with the Schrödinger equation, lends itself to interesting wider range of schemes, appropriate for superresolution and enhancement of fully textured images, by proper selection and local adaptation of the potential, introduced into the generalized scheme by the Schrödinger equation. The conflicting requirements of sharpening (i.e. edge enhancement) and filtering (i.e. noise reduction) are in this and other related studies (e.g. [19], [11]) simultaneously accomplished by invoking the smoothness assumption, i.e. a pixel is assumed to belong to either a smooth area or an edge. (This does not have to be an all-or none decision and, in fact as in this study too the diffusion coefficient or other processing parameters are a function of the gradient). This assumption, that is generally valid over a wide range of loci distributed over natural images, is violated over highly textured areas. The latter are consequently either smoothed, eliminating important features characteristic of natural images, or give rise to erroneous edges as a result of the sharpening properties of the process. The potential component of the Schrödinger equation add the extra dependent variable that can take care of fine periodic structures, characteristic of various textures, since it imposes periodic constraints on the solution. However, in such an implementation the potential has to be locally adopted to the the various texture properties distributed over the image. This extra facet of the the generalized complex scheme is currently under investigation.

Acknowledgments

This research has been supported in part by the Ollendorf Minerva Center, the Fund for the Promotion of Research at the Technion, Israel Academy of

Science, Tel-Aviv University fund, the Adams Center and the Israeli Ministry of Science.

APPENDIX

A Properties of the fundamental solution

We analyze the fundamental solution (9) to the problem stated in (4). The kernel can be separated to its real and imaginary parts. As the initial condition I_0 is real valued in this study, the real part of $I(x;t)$ is affected only by the real kernel and the imaginary part of $I(x;t)$ is affected only by the imaginary kernel:

$$I(x;t) = I_R + iI_I = I_0 * h = I_0 * h_R + iI_0 * h_I, \tag{30}$$

where $h = h_R + ih_I$. (we get $I_R = I_0 * h_R$, $I_I = I_0 * h_I$).

The nature of the complex kernel do not change through the evolution, the kernel is basically rescaled according the the time t (or to σ). Therefore we can analyze a few characteristics of the kernel as a function of σ for different values of θ. In the following sections we give some of the major characteristics of the real and imaginary kernels. An important result is that the approximation for small θ of the real part to a Gaussian and of the imaginary part to its second derivative, scaled by time is of the order $O(\theta^2)$.

In section A.3 we give a detailed calculation of the constant dictated by the initial conditions.

A.1 Properties of h_R

$$h_R(x;t) = Ag_\sigma(x;t)\cos\alpha(x;t). \tag{31}$$

A.1.1 Operator norm

The norm (maximum amplification of the input signal) is bounded by:

$$\begin{array}{rcl} \|T_{h_R}\|_\infty & \leq & \|h_R\|_1 \text{ see section A.4 (norm of a convolution operator)} \\ & = & \int_{-\infty}^{\infty} |h_R(x)|dx \\ & = & \int_{-\infty}^{\infty} |Ag_\sigma(x)\cos\alpha(x)|dx \\ & \leq & A\int_{-\infty}^{\infty} |g_\sigma(x)|dx \\ & = & A = (\cos\theta)^{-1/2} \\ & = & 1 + \frac{\theta^2}{4} + O(\theta^4). \end{array} \tag{32}$$

A.1.2 Effectively positive kernels

One requirement of the linear scale-space is the non-creation of new local extrema along the scale-space in 1D. Kernels obeying this requirement should be positive. In 1D this is equivalent for the operator to be causal, (see Lindeberg, Romeny, "Linear scale-space", in [21]).

As this kernel is not positive at all points, we would like to check how close is it to a positive kernel. A first "positivity criterion" can be to calculate the smallest point $x_0 > 0$ where h_R is not positive, that is $h_R(x_0) = 0$. As $h_R(0) > 0$ and h_R is symmetric, this means that $h_R(x) > 0$ for all $x \in (-x_0, x_0)$.

$$\begin{array}{rcl} h_R(x_0) & = & Ag_\sigma(x_0)\cos\alpha(x_0) = 0 \\ \Rightarrow & & \cos\alpha(x_0) = 0 \\ \Rightarrow & & \alpha(x_0) = \frac{x_0^2 \sin\theta}{4tr} - \frac{\theta}{2} = \frac{\pi}{2} \\ x_0 & = & \sqrt{2(\pi+\theta)tr/\sin\theta} \\ & = & \sigma\sqrt{(\pi+\theta)\cot\theta} \quad (\sigma^2 = 2tr/\cos\theta). \end{array} \tag{33}$$

For example, for $\theta = 1^\circ = \frac{\pi}{180}$ we get $x_0 = 13.4\sigma$.

Trying to be more precise in measuring the relation between h_R and a positive kernel we define a positivity measure $-1 \leq P_h \leq 1$ of a kernel h as follows:

$$P_h \doteq \frac{\int_{-\infty}^{\infty} h(x)dx}{\int_{-\infty}^{\infty} |h(x)|dx}. \tag{34}$$

We would like to determine the conditions for h_R to be effectively positive, that is $1 - \epsilon \leq P_{h_R} \leq 1$.

In order to give some bound on P_{h_R} let us first find a point $x_1 > 0$ where $\cos\alpha(x_1) = 0.5$:

$$\begin{array}{lcll} \cos\alpha(x_1) & = & \frac{1}{2} \quad \Rightarrow & \\ \alpha(x_1) & = & \frac{x_1^2 \sin\theta}{4tr} - \frac{\theta}{2} = \frac{\pi}{3} \quad \Rightarrow & \\ x_1 & = & \sqrt{\frac{2}{3}(2\pi + 3\theta)tr/\sin\theta} & \\ & = & \sigma\sqrt{(\frac{2}{3}\pi + \theta)\cot\theta} & (\sigma^2 = 2tr/\cos\theta). \end{array} \tag{35}$$

For this bound we assume $x_1 > \sigma$, so it is valid for $1.28_{rad} = 73^\circ > \theta > 0$. We use the relations:

$$\begin{array}{ll} (*) & -\int_{x_1}^{\infty} g_\sigma(x)dx \le \int_{x_1}^{\infty} g_\sigma(x)\cos\alpha(x)dx \le \int_{x_1}^{\infty} g_\sigma(x)dx \\ & (\text{as } -1 \le \cos\alpha(x) \le 1, \quad g_\sigma > 0), \\ (**) & \frac{1}{8} \le \frac{1}{2}\int_0^{\sigma} g_\sigma(x)dx \le \frac{1}{2}\int_0^{x_1} g_\sigma(x)dx \le \int_0^{x_1} g_\sigma(x)\cos\alpha(x)dx \\ & (\text{as } \cos\alpha(x) \ge \frac{1}{2} \text{ for all } x \in [0, x_1] \text{ , and } x_1 > \sigma). \end{array}$$

$$\begin{array}{lcll} P_{h_R} & = & \frac{\int_{-\infty}^{\infty} h_R(x)dx}{\int_{-\infty}^{\infty} |h_R(x)|dx} & \\ & = & \frac{\int_0^{\infty} g_\sigma(x)\cos\alpha(x)dx}{\int_0^{\infty} |g_\sigma(x)\cos\alpha(x)|dx} & \text{(symmetric kernel)} \\ & = & \frac{\int_0^{x_1} g_\sigma(x)\cos\alpha(x)dx + \int_{x_1}^{\infty} g_\sigma(x)\cos\alpha(x)dx}{\int_0^{x_1} |g_\sigma(x)\cos\alpha(x)|dx + \int_{x_1}^{\infty} |g_\sigma(x)\cos\alpha(x)|dx} & \\ & = & \frac{1 + \frac{\int_{x_1}^{\infty} g_\sigma(x)\cos\alpha(x)dx}{\int_0^{x_1} g_\sigma(x)\cos\alpha(x)dx}}{1 + \frac{\int_{x_1}^{\infty} |g_\sigma(x)\cos\alpha(x)|dx}{\int_0^{x_1} g_\sigma(x)\cos\alpha(x)dx}} & \\ & \ge & \frac{1 - \frac{\int_{x_1}^{\infty} g_\sigma(x)dx}{\int_0^{x_1} g_\sigma(x)\cos\alpha(x)dx}}{1 + \frac{\int_{x_1}^{\infty} g_\sigma(x)dx}{\int_0^{x_1} g_\sigma(x)\cos\alpha(x)dx}} & (*) \\ & \ge & \frac{1 - 8\int_{x_1}^{\infty} g_\sigma(x)dx}{1 + 8\int_{x_1}^{\infty} g_\sigma(x)dx} & (**) \\ & = & \frac{1 - 8\Phi(-x_1/\sigma)}{1 + 8\Phi(-x_1/\sigma)} & \end{array} \tag{36}$$

where

$$\Phi(x) = \int_{-\infty}^{x} g_{\sigma=1}(s)ds \tag{37}$$

Example (a): for $\theta = 1^\circ = \frac{\pi}{180}$ we get $x_1 = 11\sigma$, and $P_{h_R} \ge \frac{1-8\Phi(-11)}{1+8\Phi(-11)} = 1 - 2 * 10^{-27}$.

Example (b): for $P_{h_R} > 0.99999, \quad (\epsilon < 10^{-5})$ we require $\theta < 5^\circ$.

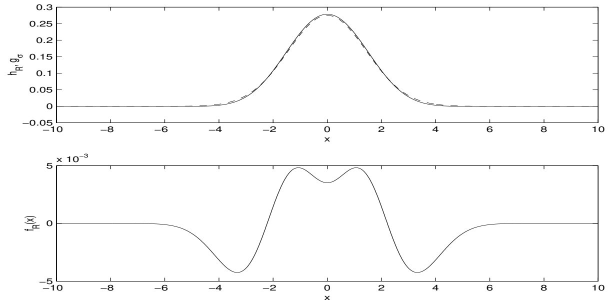

Figure 14: Top: h_R (full line) and g_σ (dashed line) as a function of x. Bottom: The difference function $f_R = h_R - g_\sigma$. $\theta = \frac{\pi}{10}$.

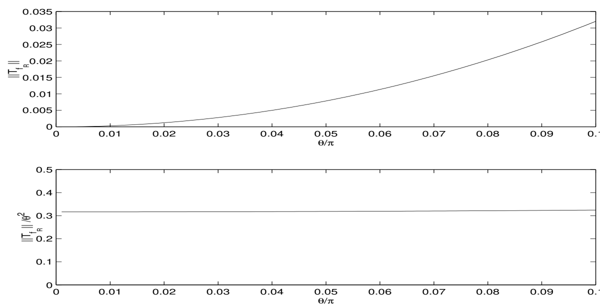

Figure 15: Top: d_R, bottom d_R/θ^2 as a function of θ, $(t = 1)$.

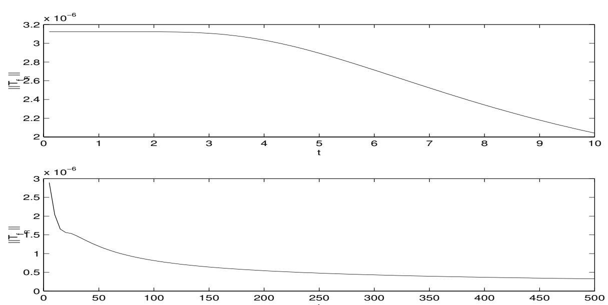

Figure 16: d_R as a function of t, $(\theta = \pi/1000)$. Top: $t \in (0, 10)$, bottom $t \in (5, 500)$.

A.1.3 Distance between h_R and a Gaussian

Let us denote f_R as the difference function between h_R and a Gaussian at time t (see Fig. 14):

$$f_R(x;t) = h_R(x;t) - g_\sigma(x;t). \tag{38}$$

We define the distance between h_R and g_σ as the norm of the convolution operator with kernel f_R, that is:

$$d(h_R, g_\sigma) \doteq d_R \doteq \|T_{f_R}\|_\infty \tag{39}$$

First we will obtain the order of this distance as a function of theta:

$$\begin{aligned}
d_R &= \|T_{f_R}\|_\infty \leq \|f_R\|_1 = \textstyle\int_{-\infty}^{\infty} |h_R(x) - g_\sigma(x)|dx \\
&= \textstyle\int_{-\infty}^{\infty} |Ag_\sigma(x)\cos\alpha(x) - g_\sigma(x)|dx \\
&= 2\textstyle\int_0^\infty |A\cos(\frac{x^2\sin\theta}{4tr} - \frac{\theta}{2}) - 1|g_\sigma(x)dx \\
&= 2\textstyle\int_0^\infty |A\cos(\frac{x^2\tan\theta}{2\sigma^2} - \frac{\theta}{2}) - 1|g_\sigma(x)dx \\
&= 2\textstyle\int_0^a |A\cos(\frac{x^2\tan\theta}{2\sigma^2} - \frac{\theta}{2}) - 1|g_\sigma(x)dx + 2\int_a^\infty |A\cos(\frac{x^2\tan\theta}{2\sigma^2} - \frac{\theta}{2}) - 1|g_\sigma(x)dx \\
&< 2\textstyle\int_0^a |A\cos(\frac{x^2\tan\theta}{2\sigma^2} - \frac{\theta}{2}) - 1|g_\sigma(x)dx + 2(A+1)\int_a^\infty g_\sigma(x)dx \\
&< 2\max_{x\in[0,a]}[|A\cos(\frac{x^2\tan\theta}{2\sigma^2} - \frac{\theta}{2}) - 1|]\textstyle\int_0^a g_\sigma(x)dx + 4A\Phi(-a/\sigma) \\
&< 2\max_{x\in[0,a]}[|A\cos(\frac{x^2\tan\theta}{2\sigma^2} - \frac{\theta}{2}) - 1|] + 4A\Phi(-a/\sigma)
\end{aligned} \tag{40}$$

Let us choose $a = \sqrt{n}\sigma$ such that $n > 1$ and $\alpha(a) \ll \frac{\pi}{2}$ (therefore $\cos(\alpha(x)) > 0$ for any $x \in [0,a]$). Recalling that $\tan\theta = \theta + O(\theta^3)$ and $A = 1 + O(\theta^2)$ we get

$$\begin{aligned}
&\max_{x\in[0,a]}[|A\cos(\tfrac{x^2\tan\theta}{2\sigma^2} - \tfrac{\theta}{2}) - 1|] \\
&= \max\{\max_{x\in[0,a]}(A\cos(\tfrac{x^2\tan\theta}{2\sigma^2} - \tfrac{\theta}{2}) - 1), \max_{x\in[0,a]} -(A\cos(\tfrac{x^2\tan\theta}{2\sigma^2} - \tfrac{\theta}{2}) - 1)\} \\
&= \max\{(\max_{x\in[0,a]}(A\cos(\tfrac{x^2\tan\theta}{2\sigma^2} - \tfrac{\theta}{2})) - 1), (1 - \min_{x\in[0,a]}(A\cos(\tfrac{x^2\tan\theta}{2\sigma^2} - \tfrac{\theta}{2})))\} \\
&= \max\{(A-1), (1 - (A\cos(\tfrac{a^2\tan\theta}{2\sigma^2} - \tfrac{\theta}{2})))\} \\
&= \max\{(A-1), (1 - A\cos(\tfrac{n\tan\theta}{2} - \tfrac{\theta}{2}))\} \\
&= \max\{(A-1), (1 - A\cos(\tilde{n}\theta + O(\theta^3)))\} \\
&= \max\{O(\theta^2), (1 - (1+O(\theta^2))(1 - \tilde{n}^2\theta^2/2 + O(\theta^4)))\} \\
&= O(\theta^2).
\end{aligned} \tag{41}$$

The term $\Phi(-a/\sigma) = \Phi(-\sqrt{n})$ decays exponentially with the growth of n. Therefore we conclude that

$$d_R = O(\theta^2) \tag{42}$$

The exact analytical expression of d_R is a complicated function of θ and t. Therefore we show graphically a bound on d_R as a function of θ (Fig. 15) and its behavior as a function of time (Fig. 16) (to which we have no analytical expression). Main results:

$$d_R < 0.5\theta^2, \quad \forall\theta \in (0, \frac{\pi}{10}), \forall t \tag{43}$$

$$d_R(t_0) > d_R(t_1), \quad \forall t_1 > t_0 > 0, \forall\theta \in (0, \frac{\pi}{10}) \tag{44}$$

The approximation error decreases in proportion to θ^2 (for small θ) and decreases monotonically with time.

A.1.4 Definite integral of h_R

$$\int_{-\infty}^{\infty} h_R(x;t)dx = 1 \tag{45}$$

for all θ, t (follows directly from section A.3).

A.2 properties of h_I

A.2.1 small theta approximation from fundamental solution

The second derivative of a Gaussian (in 1D) is:

$$\begin{aligned} \frac{\partial^2}{\partial x^2} g_\sigma(x) &= \frac{\partial^2}{\partial x^2} C e^{-x^2/2\sigma^2} \text{ ,where } C = \frac{1}{\sqrt{2\pi}\sigma(t)} \\ &= \frac{\partial}{\partial x}\big(-C\frac{x}{\sigma^2}e^{-x^2/2\sigma^2}\big) \\ &= C\frac{x^2-\sigma^2}{\sigma^4}e^{-x^2/2\sigma^2}. \end{aligned} \tag{46}$$

Small theta approximation of h_I:

$$\begin{aligned} h_I &= A g_\sigma(x;t)\sin\alpha(x;t) \\ &= \frac{1}{\sqrt{\cos\theta}} C e^{-x^2/2\sigma^2} \sin\big(\frac{x^2\sin\theta}{4tr} - \frac{\theta}{2}\big) \\ &\approx C e^{-x^2/2\sigma^2} \sin\big(\frac{x^2\theta}{4tr} - \frac{\theta}{2}\big) \qquad (\sqrt{\cos\theta} \approx 1 \quad , \sin\theta \approx \theta) \\ &\approx C e^{-x^2/2\sigma^2} \big(\frac{\theta(x^2-2tr)}{4tr}\big) \qquad \big(\sin(\frac{x^2\theta}{4tr} - \frac{\theta}{2}) \approx (\frac{x^2\theta}{4tr} - \frac{\theta}{2})\big) \\ &\approx C e^{-x^2/2\sigma^2} \big(\frac{\theta(x^2-\sigma^2)}{2\sigma^2}\big) \qquad (\sigma^2 = 2tr/\cos\theta \approx 2tr) \\ &= C\frac{x^2-\sigma^2}{\sigma^4} e^{-x^2/2\sigma^2}\theta tr \\ &= \frac{\partial^2}{\partial x^2} g_\sigma(x)\theta tr. \end{aligned} \tag{47}$$

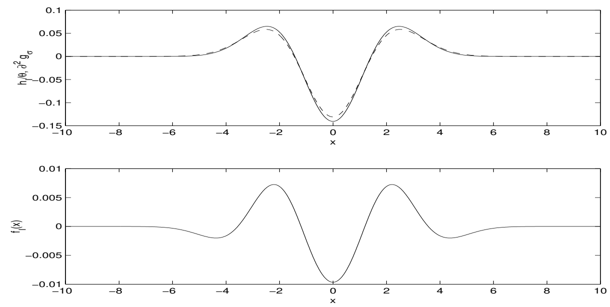

Figure 17: Top: h_I/θ (full line) and $\frac{\partial^2}{\partial x^2} g_\sigma t$ (dashed line) as a function of x. Bottom: The difference function f_I. $\theta = \frac{\pi}{10}$.

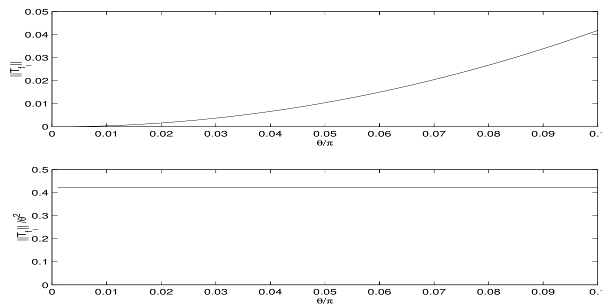

Figure 18: Top: d_I, bottom d_I/θ^2 as a function of θ, $(t = 1)$.

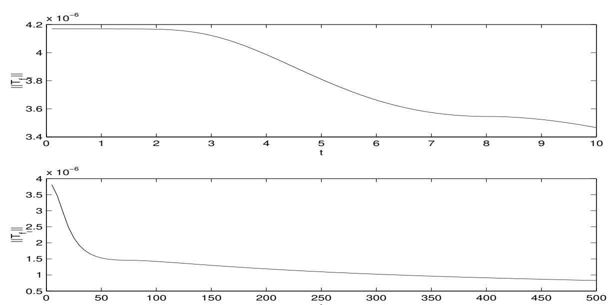

Figure 19: d_I as a function of t, $(\theta = \pi/1000)$. Top: $t \in (0, 10)$, bottom $t \in (5, 500)$.

A.2.2 Approximation error

We follow the same logic of the real part analysis. Let us denote f_I as the difference function between h_I/θ and a Gaussian's 2nd derivative scaled by time (see Fig. 17):

$$f_I(x;t) = \frac{h_I(x;t)}{\theta} - \frac{\partial^2}{\partial x^2} g_\sigma(x;t)t. \tag{48}$$

We define the distance as the norm of the convolution operator with kernel f_I:

$$d(h_I/\theta, \frac{\partial^2}{\partial x^2} g_\sigma t) \doteq d_I \doteq \|T_{f_I}\|_\infty \tag{49}$$

The analytical result follows the same arguments as in the real part section and we get

$$d_I = O(\theta^2) \tag{50}$$

The graphical results (Figs. 18, 19) lead also to similar characteristics:

$$d_I < 0.5\theta^2, \quad \forall \theta \in (0, \frac{\pi}{10}), \, \forall t. \tag{51}$$

$$d_I(t_0) > d_I(t_1), \quad \forall t_1 > t_0 > 0, \forall \theta \in (0, \frac{\pi}{10}). \tag{52}$$

We can conclude that the approximation error decreases in proportion to θ^2 (for small θ) and decreases monotonically with time.

A.2.3 Definite integral of h_I

$$\int_{-\infty}^{\infty} h_I(x;t)dx = 0 \tag{53}$$

for all θ, t (follows directly from section A.3).

A.3 Constant of the fundamental solution

The basic fundamental solution is

$$\begin{aligned} h(x;t) &= Ke^{-\frac{x^2 \cos\theta}{4tr}} e^{i\frac{x^2 \sin\theta}{4tr}} \\ &= Ke^{-\frac{x^2}{2\sigma^2}} e^{i\frac{x^2 \tan\theta}{2\sigma^2}}, \quad (\sigma^2 = \frac{2tr}{\cos\theta}) \\ &= |K|e^{i\varphi} e^{-\frac{x^2}{2\sigma^2}} e^{i\frac{x^2 \tan\theta}{2\sigma^2}} \\ &= |K|e^{-\frac{x^2}{2\sigma^2}} e^{i\left(\frac{x^2 \tan\theta}{2\sigma^2} + \varphi\right)} \end{aligned} \tag{54}$$

As the constant K is complex, there are two degrees of freedom: the magnitude $|K|$ and the phase φ. The initial condition dictates:

$$\begin{array}{ll} (a) & \int_{-\infty}^{\infty} h(x;t\to 0)dx = 1, \\ (b) & \int_{|x|>\epsilon} |h(x;t\to 0)|dx \to 0, \quad \text{where } \epsilon = \epsilon(t\to 0)\to 0. \end{array} \tag{55}$$

From (55.a) we require

$$\begin{array}{lll} (a.I) & \int_{-\infty}^{\infty} h_R(x;t\to 0)dx & = 1 \\ (a.II) & \int_{-\infty}^{\infty} h_I(x;t\to 0)dx & = 0. \end{array} \tag{56}$$

We will see that (55.b) is satisfied readily from the Gaussian properties.

First, let us find the definite integral of h_R. We use the following definite integral formula (taken from [20] p. 459, Eq. 16):

$$\begin{array}{l} \int_{-\infty}^{\infty} e^{-ax^2+bx+c}\{\sin|\cos\}(px^2+qx+r)dx = \\ \frac{\sqrt{\pi}}{(a^2+p^2)^{1/4}} \exp\left[\frac{a(b^2-4ac)-(aq^2-2bpq+4cp^2)}{4(a^2+p^2)}\right]\{\sin|\cos\}\left[\frac{1}{2}\arctan\frac{p}{a} - \frac{p(q^2-4pr)-(b^2p-2abq+4a^2r)}{4(a^2+p^2)}\right] \end{array} \tag{57}$$

From (54) we write h_R as

$$\begin{array}{rcl} h_R & = & |K|e^{-\frac{x^2}{2\sigma^2}}\cos\left(\frac{x^2\tan\theta}{2\sigma^2}+\varphi\right) \\ & = & |K|e^{-ax^2}\cos\left(px^2+\varphi\right) \\ & & \text{where } a = \frac{1}{2\sigma^2}, \quad p = \frac{\tan\theta}{2\sigma^2}. \end{array} \tag{58}$$

From (57) and (58) we get:

$$\begin{array}{l} \int_{-\infty}^{\infty} h_R(x)dx = \\ |K|\int_{-\infty}^{\infty} e^{-ax^2}\cos\left(px^2+\varphi\right)dx = \\ = |K|\frac{\sqrt{\pi}}{(a^2+p^2)^{1/4}}\cos\left[\frac{1}{2}\arctan\frac{p}{a}+\varphi\right] \\ = |K|\frac{\sqrt{2\pi}\sigma}{(1+\tan^2\theta)^{1/4}}\cos\left(\frac{1}{2}\theta+\varphi\right) \\ = |K|\sqrt{2\pi\cos\theta}\sigma\cos\left(\frac{1}{2}\theta+\varphi\right). \end{array} \tag{59}$$

Similarly

$$\begin{array}{l} \int_{-\infty}^{\infty} h_I(x)dx = \\ |K|\int_{-\infty}^{\infty} e^{-ax^2}\sin\left(px^2+\varphi\right)dx = \\ = |K|\sqrt{2\pi\cos\theta}\sigma\sin\left(\frac{1}{2}\theta+\varphi\right). \end{array} \tag{60}$$

From (56.$a.II$) and (60) we get

$$\varphi = -\frac{1}{2}\theta \quad , \tag{61}$$

from $(56.a.I)$ and (59) we get

$$|K| = \frac{1}{\sqrt{2\pi\cos\theta\sigma}} \quad , \tag{62}$$

hence the constant K is

$$K = \frac{e^{-i\frac{1}{2}\theta}}{\sqrt{2\pi\cos\theta\sigma}}. \tag{63}$$

Requirement $(55.b)$ is retained due to the characteristics of the Gaussian function. Let us choose $\epsilon = \sqrt{\sigma}$. Therefore $\epsilon(t) = (2tr/\cos\theta)^{1/4} \to_{t\to 0} 0$ for any $|\theta| < \frac{\pi}{2}$. And we get

$$\begin{aligned} &\int_{|x|>\epsilon} |h(x)|dx = \\ &\int_{|x|>\epsilon} |\tfrac{1}{\sqrt{\cos\theta}} g_\sigma(x) e^{i\alpha(x)}|dx = \\ &\tfrac{2}{\sqrt{\cos\theta}} \int_{-\infty}^{-\sqrt{\sigma}} g_\sigma(x)dx = \\ &\tfrac{2}{\sqrt{\cos\theta}} \Phi(-\tfrac{1}{\sqrt{\sigma}}) \to_{\sigma\to 0} 0 \quad . \end{aligned} \tag{64}$$

In the concise writing of the fundamental solution (9) K is actually separated to 3 multiplicative parts in the expressions of A, g_σ and α. Therefore $C = 1$.

A.4 Norm of a convolution operator

Let f be a bounded function $\max(f) < M$, $(f \in L^\infty)$. Let T_h be the convolution operator with the kernel h $(h \in L^1)$: $T_h f = h * f$. We want to prove the relation

$$\|T_h\|_\infty \leq \|h\|_1. \tag{65}$$

Let us first find a bound on $\|T_h f\|_\infty$. We use Young's inequality

$$\begin{aligned} &\|f * h\|_r \leq \|f\|_p \|h\|_q, \\ &f \in L^p, g \in L^q, \quad r^{-1} = p^{-1} + q^{-1} - 1, \quad (1 \leq p, q, r \leq \infty). \end{aligned} \tag{66}$$

Setting $p = \infty, q = 1, r = \infty$ we get

$$\|T_h f\|_\infty \leq \|f\|_\infty \|h\|_1. \tag{67}$$

To get some intuition of why this is true, we show step by step, the one-dimensional case:

$$\begin{aligned}
\|T_h f\|_\infty &= \|h * f\|_\infty = \max_x |h * f| \\
&= \max_x |\int_{-\infty}^{\infty} h(x-y) f(y) dy| \\
&\leq \max_x \int_{-\infty}^{\infty} |h(x-y) f(y)| dy \\
&\leq \max_x \int_{-\infty}^{\infty} |h(x-y)| \max_y(|f(y)|) dy \\
&= \|f\|_\infty \max_x \int_{-\infty}^{\infty} |h(y)| dy \\
&= \|f\|_\infty \|h\|_1 .
\end{aligned}$$

Recalling the definition of a norm of a linear operator

$$\|T_h\|_\infty \doteq \sup_{\|f\| \neq 0} \frac{\|T_h f\|_\infty}{\|f\|_\infty}$$

we let

$$f_{sup} = \text{argsup}_{\|f\| \neq 0} \frac{\|T_h f\|_\infty}{\|f\|_\infty}$$

so that $\|T_h f_{sup}\|_\infty = \|T_h\|_\infty \|f_{sup}\|_\infty$. Using the relation of (67) we get

$$\|T_h\|_\infty \|f_{sup}\|_\infty \leq \|h\|_1 \|f_{sup}\|_\infty .$$

References

[1] L. Alvarez, L. Mazorra, "Signal and image restoration using shock filters and anisotropic diffusion", SIAM J. Numer. Anal. Vol. 31, No. 2, pp. 590-605, 1994.

[2] F. Barbaresco, "Calcul des variations et analyse spectrale: equations de Fourier et de Burgers pour modeles autoregressifs regularises", Traitement du Signal, vol. 17, No. 5/6, 2000.

[3] P.J. Burt, E.H. Adelson, "The Laplacian pyramid as a compact image code", IEEE Trans. Commun., vol. COM-31, No. 4, pp.532-540, 1983.

[4] F. Catte, P. L. Lions, J. M. Morel and T. Coll, "Image selective smoothing and edge detection by nonlinear diffusion", SIAM J. Num. Anal., vol. 29, no. 1, pp. 182-193, 1992.

[5] O. Coulon, S.R. Arridge, "Dual echo MR image processing using multi-spectral probabilistic diffusion coupled with shock filters", MIUA'2000, British Conference on Medical Image Understanding and Analysis, London, United-Kingdom, 2000.

[6] M.C. Cross, P.C. Hohenberg, "Pattern formation outside of equilibrium", Rev. Modern Phys. 65, 854-1090 (1993).

[7] V. L. Ginzburg and L. D. Landau, Zh. Eksp. Teor. Fiz. 20, 1064 (1950); English translation: see Men of Physics: Landau, Vol. II, edited by D. ter Haar, Pergamon, New York, 1965, pp. 546-568.

[8] G. Gilboa, Y.Y. Zeevi, N. Sochen, "Complex diffusion processes for image filtering", Michael Kerckhove (Ed.): Scale-Space 2001, LNCS 2106, pp. 299-307, Springer-Verlag 2001.

[9] G. Gilboa, N. Sochen, Y.Y. Zeevi, "Regularized shock filters and complex diffusion", ECCV-'02, LNCS 2350, pp. 399-313, Springer-Verlag 2002.

[10] G. Gilboa, N. Sochen, Y.Y. Zeevi, "Image enhancement segmentation and denoising by time dependent nonlinear diffusion processes", Proc. Int. Conf. on Image Processing (ICIP) 2001, vol. 3, pp. 134-137, Greece 2001.

[11] G. Gilboa, N. Sochen, Y.Y. Zeevi, "A Forward-and-Backward Diffusion Process for Adaptive Image Enhancement and Denoising", to appear on IEEE Transactions on Image Processing, July 2002.

[12] F. Guichard, J-M. Morel, "A note on two classical shock filters and their asymptotics", M. Kerckhove (Ed.): Scale-Space 2001, LNCS 2106, pp. 75-84, Springer-Verlag 2001.

[13] M. Kerckhove (Ed.), "Scale-Space and morphology in computer-vision", Scale-Space 2001, LNCS 2106, Springer-Verlag 2001.

[14] J.J. Koenderink, "The structure of images", *Biol. Cybern.*, 50: 363-370, 1984.

[15] P. Kornprobst, R. Deriche, G. Aubert, "Image coupling, restoration and enhancement via PDE's", Proc. Int. Conf. on Image Processing 1997, pp. 458–461, Santa-Barbara (USA), 1997.

[16] M. Nagasawa, *S*chrödinger equations and diffusion theory, Monographs in mathematics, vol. 86, Birkhäuser Verlag, Basel, Switzerland 1993.

[17] A.C. Newell, "Envelope equations", Lect. in Appl. Math. 15, pp. 157-163, 1974.

[18] S.J. Osher and L. I. Rudin, "Feature-oriented image enhancement using shock filters", SIAM J. Numer. Anal. 27, pp. 919-940, 1990.

[19] P. Perona and J. Malik, "Scale-space and edge detection using anisotropic diffusion", IEEE Trans. Pat. Anal. Machine Intel., vol. PAMI-12,no. 7, pp. 629-639, 1990.

[20] A.P. Prudnikov, Y.A. Brychkov, O.I. Marichev, "Integrals and series", (English translation by N.M Queen), Vol. I, Gordon and Breach, 1986.

[21] B M ter Haar Romeny Ed., *Geometry Driven Diffusion in Computer Vision*, Kluwer Academic Publishers, 1994.

[22] F. Ratliff, *Mach bands: quantitative studies on neural networks in the retina*, Holden-Day, San Francisco (1965).

[23] N.Rougon, F.Preteux, "Controlled anisotropic diffusion", Proc. SPIE Conf. on Nonlinear Image Processing VI - IS&T / SPIE Symp. on Electronic Imaging, Science and Technology '95, San Jose, CA, Vol. 2424, 1995, pp. 329-340.

[24] A. P. Witkin, "Scale space filtering", Proc. Int. Joint Conf. On Artificial Intelligence, pp. 1019-1023, 1983.

[25] A. L. Yuille and T. Poggio, "Fingerprint theorems for zero crossings", J. Opt. Soc. Am. A, vol. 2, no. 5, pp. 683-692, 1985.